Transition metal AB_3 intermetallics: Structure maps based on quantum mechanical stability

Peter Michael Clark, Stephen Lee[*], Daniel C. Fredrickson

Baker Laboratory, Department of Chemistry and Chemical Biology, Cornell University, Room 160B, S. T. Olin Building, Ithaca, NY 14853-1301, USA

Abstract

We study a two-dimensional structure map for AB_3 binary transition metal compounds with variables appropriate for direct quantum-mechanical energy calculations. The variables are the electron count and ΔH_{ii}, the difference in d-orbital Coulombic integrals. The experimental structure map differentiates between the six known AB_3 transition metal structure types: Cr_3Si, $AuCu_3$, $SnNi_3$, $TiAl_3$, $TiCu_3$ and $TiNi_3$. The theoretical quantum mechanical map (based on μ_2-Hückel calculations) gives good agreement with the experimental map.

The numerical accuracy of the μ_2-Hückel energies is assessed by direct comparison to LDA-DFT calculations carried out on $TaIr_3$. For this system, both the μ_2-Hückel and LDA-DFT calculations place the six structure types in the same energetic order. The μ_2-Hückel theory, in addition, allows further analysis on the structural origins of these differences in energy. The chief structural features responsible for differences in energy prove to be the varying number of three- and four-member rings of bonded atoms. These results help delineate the principal factors responsible for transition metal icosahedral, Frank–Kasper vs. closest-packed structures.

1. Introduction

Structure maps have become one of the essential tools of solid-state chemists for understanding the structures of stoichiometrically homologous compounds [1–16]. In ordinary usage, the chemist considers a few atomic variables (often two) and then explores how these variables can be used to sort out, rationalize and in some cases even predict the crystal structure type of a particular phase [17–23]. In this endeavor, great attention must be paid to the variables chosen. Of course they need to make intuitive chemical sense. But to understand the exact energetic role of each variable, it is also especially useful if the variables in question can be directly incorporated into an energy calculation. For such energy calculations explicit use of quantum mechanics and of a Hamiltonian is often required.

The search for variables which the practicing chemist can find in standard tables and for which the theorist can discern a direct role in the Hamiltonian is a surprisingly complex one. That this is so, can be seen by the structure maps which have been created on the basis of quantum calculations alone. For the most part, quantum mechanically based structure maps are maps in which the variables considered are derived from quantum mechanics, but no algorithm is given as to how these same variables can be used to calculate an exact quantum mechanical energy [24–30]. Those theorists who have produced maps based on electronic energies have often relied on just a single variable, often the total number of valence electrons or the volume of the system, and, thus, either achieve only a partial

*Corresponding author. Fax: +1 607 255 4727.

E-mail address: sl137@cornell.edu (S. Lee).

separation between known structure types or must limit the range of compounds considered [31–33].

Even fewer are those structure maps which plot the difference in energy as a function of two quantum mechanical variables. Among these is the landmark study by Pettifor and Podloucky [34] on binary AB transition metal-main group compounds. In this work, Pettifor and Podloucky produced a sorting of AB structures based on the differences of their tight-binding band energy. But as an examination of their work shows, the resultant quantum-mechanical map can be used only qualitatively to understand the experimental structure map (they are shown side by side with different variables in their paper).

The difficulty here is that in ab initio quantum theory, the theory most often used in examining the differences in energy between structures, electronic energies are produced as a function of an exact chemical system. It is therefore hard to discern two variables which capture the complexity of the full chemical system. Far easier is it to find a small number of determinate variables in the context of model or semi-empirical methods. Here, by definition the model has simplified the number of variables which need be considered. It is not an accident that in the Pettifor and Podloucky work previously discussed, a semi-empirical tight-binding Hamiltonian was applied.

In this paper, we develop a two-dimensional structure map for AB_3 binary transition metal solids (where A and B are both transition elements). Unlike previous maps for AB_3 structure maps, the map variables can be directly input into standard semi-empirical band calculations. The variables considered are the average number of valence electrons per atom (electrons/atom) and the difference in d-orbital energy between the two atoms ($\Delta H_{ii} = H_{ii}(A) - H_{ii}(B)$), where H_{ii} refers to the atomic d-orbital energy). Based on these two variables, we calculate the difference in energy between the six commonly observed transition metal AB_3 solids (Fig. 1): Cr_3Si, $AuCu_3$, $SnNi_3$, $TiAl_3$, $TiCu_3$ and $TiNi_3$.

The first of these compounds is the simplest of all icosahedral phases while the remaining five are all variants of a closest packing. We determine which of these six structure types is preferred for a given value of electrons/atom and ΔH_{ii}. We then directly compare this structure map with the structure type of the known atomically ordered (but magnetically unordered) AB_3 solids. There are 35 such experimentally observed phases, and as we show, there is good agreement between the quantum mechanical energy map and the structure type which is actually observed.

We further study the structural features which cause the differences between the icosahedral Cr_3Si and closest packed $AuCu_3$ phases. Using the moment method, we
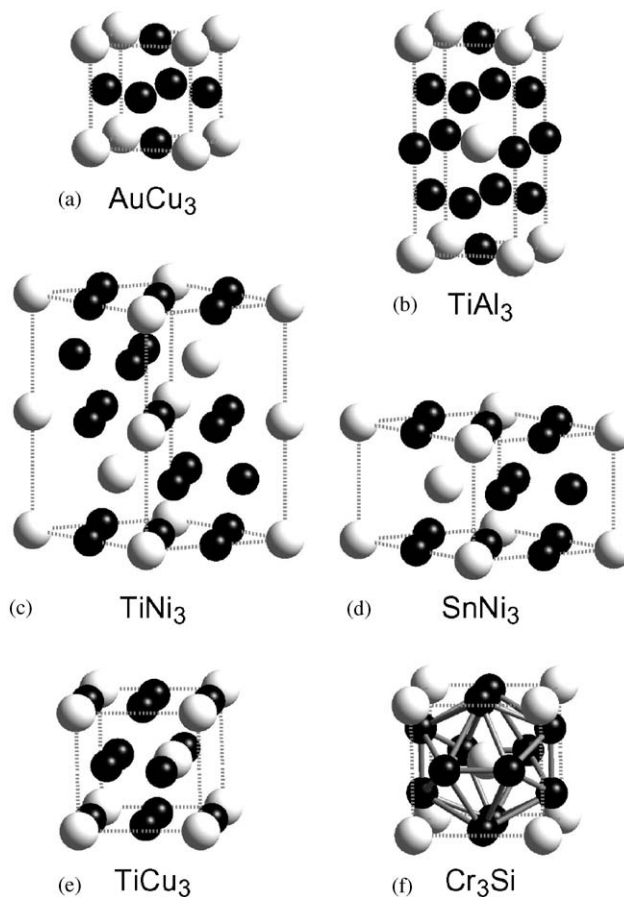

Fig. 1. The common AB_3 structure types discussed in this paper: (a) $AuCu_3$, (b) $TiAl_3$, (c) $TiNi_3$, (d) $SnNi_3$, (e) $TiCu_3$, and (f) Cr_3Si structure types. A atoms: white spheres, B atoms: black spheres.

show that within the context of tight-binding band theory, the key structural features are the different numbers of triangles and four-member rings of bonded atoms in the different structures [35,36]. This result may help account for the electron counting rules which in general differentiate closest packing from icosahedral phases.

2. Technical procedures

2.1. Tight-binding band calculations

In the tight-binding method used in this paper, the total energy E_T is expressed by

$$E_T = U(r) - V(r), \qquad (1)$$

where $U(r)$ is a hard-core interatomic repulsion energy, $V(r)$ is an attractive bonding energy, and r is a parameter dependent on the size of the system. The

total energy E_T can also be given as

$$E_T = \gamma \int_{-\infty}^{\infty} (E - E_{ave})^2 \rho(E, r) \, dE$$
$$+ \int_{-\infty}^{E_F} E \rho(E, r) \, dE, \qquad (2)$$

where the above integrals represent the repulsive and the attractive energies, respectively. Here $\rho(E, r)$ is the electronic density of the valence bands, E_F is the Fermi energy, E_{ave} is the average energy of the electronic density of states, and γ is a proportionality constant. The density $\rho(E, r)$ is found from the diagonalization of the Hamilton matrix.

Rather than explicitly calculating γ, we use the second moment scaling approximation. As has been shown elsewhere [9,37], the difference in energy between two structures C and D is approximately

$$E_T(C) - E_T(D) = \int_{-\infty}^{E_F} E \rho_C(E, r_{expt}) \, dE$$
$$- \int_{-\infty}^{E_F} E \rho_D(E, r_{scaled}) \, dE, \qquad (3)$$

where the size of the D system has been scaled so that,

$$\int_{-\infty}^{\infty} (E - E_{ave})^2 \rho_C(E, r_{expt}) \, dE$$
$$= \int_{-\infty}^{\infty} (E - E_{ave})^2 \rho_D(E, r_{scaled}) \, dE. \qquad (4)$$

As Eqs. (3) and (4) imply, under such scaling conditions, the repulsive energy cancels and the difference in energy between the two structures is the difference in the attractive energies.

Diagonal elements, H_{ii}, are set equal to prescribed Coulombic integral values, while off-diagonal elements are based on the Wolfsberg–Helmholtz approximation, $H_{ij} = \frac{1}{2} K S_{ij} (H_{ii} + H_{jj})$. The parameter K is set to 1.75 and orbitals are assumed to be single and double ζ expansion Slater-type orbitals. For AB_3 binary transition metal systems, parameters are needed for both the A and B elements. We used the same ζ Slater-type coefficients for both the A and B atoms. We assumed the difference in Coulombic integrals of the A and B s, p, and d are the same. We therefore reduce the difference between the A and B atoms into a single parameter $\Delta H_{ii} = H_{ii}(A) - H_{ii}(B)$ where $H_{ii}(A)$ and $H_{ii}(B)$ refer to the Coulombic integrals for the A and B atoms. The atomic parameters are the same ones used effectively in previous work on transition metal alloys [38]. These parameters were initially developed for extended Hückel calculations involving Fe. The parameters include $H_{ii}(4s) = -9.10$ eV, $H_{ii}(4p) = -5.32$ eV, $H_{ii}(3d) = -12.60$ eV; $\zeta(4s) = \zeta(4p) = 1.9$, $\zeta_1(3d) = 5.35$ (0.5505), and $\zeta_2(3d) = 2.00$ (0.6260). In all cases the r_{expt} was based

on the value for the Ti–Ni system, a system that crystallizes in the $TiNi_3$ structure type.

2.2. Literature survey of AB_3 phases

The tight-binding calculations reported in this paper are for AB_3 binary transition metals. Such calculations assume complete atomic ordering between the two binary elements. Energies and not free energies are calculated. No spin terms are included in the Hamiltonian. These calculational requirements place strong constraints on the type of experimental systems considered. The above conditions suggest that we should consider only perfectly atomically ordered, magnetically unordered binary transition metal systems stable at absolute zero temperature. However, few phase diagrams extend to temperatures below a few hundred degrees Celsius. We therefore considered all systems found at the low-temperature regime of existing phase diagrams. We examined all binary phase diagrams involving pairs of d-block transition metal elements. Transition metal atoms are taken here to belong to elements between groups 4 and 10 of the periodic table. We consider only atomically ordered phases where the stoichiometry was of AB_3 type (A and B being the two transition metal atoms).

In this paper we are interested in phases with no known magnetic ordering, i.e., in phases which are not ferromagnetic, ferrimagnetic, antiferromagnetic or contain spin-waves. We therefore reviewed the data in the Landolt–Börnstein compendium of magnetic data and ruled out all phases which are known to exhibit any of the above cooperative magnetic phenomena [39]. Such considerations exclude many phases and especially those containing the later first row transition metal elements: Cr, Mn, Fe, Co, and Ni. Indeed, only 35 AB_3 low-temperature transition metal phases proved to be atomically ordered but at the same time magnetically disordered. These are listed according to structure type in Table 1.

2.3. Tabulation of tight-binding Coulombic integrals

In order to directly compare known AB_3 phases with the band calculation results we need to determine, first, the average number of valence electrons per atom in the AB_3 system and, second, the value for ΔH_{ii}. The former may be directly determined from the atomic number of the elements. For the latter we turned to standard compendiums of extended Hückel parameters for transition metal elements. These in turn are based on tabulated numerical fits to Hartree–Fock and relativistic Hartree–Fock calculations. Unfortunately, we could find few complete tabulations which included all the transition metal elements; some adjustments to tabulated lists were therefore required. In this paper, we

Table 1
Stable transition metal AB_3 compounds

AuCu$_3$	SiCr$_3$	SnNi$_3$	TiAl$_3$	TiCu$_3$	TiNi$_3$
CoPt$_3$	CoV$_3$	MoIr$_3$	NbPd$_3$	MoNi$_3$	HfPt$_3$
HfIr$_3$	IrCr$_3$	WIr$_3$	TaPd$_3$	NbNi$_3$	TiNi$_3$
HfPd$_3$	IrMo$_3$		VNi$_3$		TiPd$_3$
HfPt$_3$	IrTi$_3$		VPt$_3$		TiPt$_3$
HfRh$_3$	IrV$_3$				ZrPd$_3$
NbIr$_3$	NiV$_3$				
NbRh$_3$	OsMo$_3$				
NbRu$_3$	OsNb$_3$				
TaIr$_3$	PdV$_3$				
TiIr$_3$	PtV$_3$				
TaRh$_3$	RhNb$_3$				
TiRh$_3$	RhV$_3$				
VIr$_3$					
ZrIr$_3$					
ZrPt$_3$					

Table 2
d orbital H_{ii} values for the *d*-block elements

Element	*d* H_{ii} (eV)	Element	*d* H_{ii} (eV)	Element	*d* H_{ii} (eV)
Sc	−6.35	Y	−6.80	Lu	−6.62
Ti	−8.04	Zr	−8.46	Hf	−8.14
V	−9.55	Nb	−10.00	Ta	−9.57
Cr	−10.91	Mo	−11.54	W	−10.96
Mn	−12.27	Tc	−13.08	Re	−12.35
Fe	−13.54	Ru	−14.62	Os	−13.74
Co	−14.77	Rh	−16.16	Ir	−15.14
Ni	−15.97	Pd	−17.70	Pt	−16.53
Cu	−17.19	Ag	−19.24	Au	−17.92
Zn	−18.29	Cd	−20.78	Hg	−19.43

adopt the *d*-orbital H_{ii} parameters based on the extended Hückel program YAeHMOP [40].

The YAeHMOP list of parameters is complete and within individual rows of the periodic table follows chemical intuition. For instance the first row $H_{ii}(d)$ range from −11.04 eV for Ti, to −15.27 eV for Mn, and to −20.19 eV for Cu. There is a similar trend in $H_{ii}(d)$ values for the second and third row: −8.46 and −8.14 eV for, respectively, Zr and Hf; −13.54 and −13.74 eV for Fe and Os; and −19.24 and −17.92 eV for Ag and Au. However, the values between rows appear not to follow chemical intuition. As these values show, the Cu *d*-orbital is lower in energy than the Ag or Au *d*-orbital. Yet the *d*-orbital in copper is valence-like (Cu(II) is a common oxidation state) while the *d*-orbital in Ag has more core character (it is difficult to further oxidize the silver atom past Ag(I)).

After checking other references for other common extended Hückel parameters, we therefore corrected the first row transition metal values by adding 3 eV across the series. This correction is only an approximation. Further improvements can be envisaged. For example, with this correction the *d*-orbital energies of Cr, Mo and W are all approximately the same. Our intuition is that as higher oxidation states of Mo and W are more common, that their *d*-orbital energies should be higher. Table 2 gives the final if somewhat unsatisfying tabulated values for the various elements.

2.4. Equations used in method of moments

It is possible to ascertain many of the energetic features of the valence electronic density through study of the moments, μ_n, where $\mu_n = \int_{-\infty}^{\infty} E^n \rho(E)\, \mathrm{d}E$ and $\rho(E)$ is the valence electronic density of states. As some earlier publications contain a number of typographical errors, it is useful to review the equations used in the current

article. In this regard, please note that all equations below assume the $\rho(E)$ function has a total area of one, i.e., $\mu_0 = 1$.

One can reconstruct $\rho(E)$ from knowledge of the full μ_n sequence [36,41]. The μ_n where *n* is a small integer prove most important to this reconstruction. In the scaled tight-binding band calculations used in this paper, μ_0, μ_1, and μ_2 are invariant. It is most convenient to therefore consider only density of states which are in standard normal form, i.e., where μ_0, μ_1, and μ_2 are, respectively, one, zero and one. The moments of such standard normal densities of states can be established by appropriate choice of the energy unit and a judicious choice for the zero energy, see Appendix A.

As μ_0, μ_1, and μ_2 are invariant, the most important moments controlling the full density of states are μ_3 and μ_4. Experience shows the values of the third and fourth moments are particularly informative when using the above-defined standard normal $\rho(E)$ functions. The third moment gives a measure of the skewness or asymmetry in the $\rho(E)$ function while the fourth moment gives some measure of the "peakedness" of $\rho(r)$. (Later though in both this section and Appendix B, we will discuss an even better measure of the peakedness, the kurtosis.)

With two normalized density of states, $\rho_{\mathrm{I}}(E)$ and $\rho_{\mathrm{II}}(E)$, if $\rho_{\mathrm{I}}(E)$ has the more negative μ_3 value, then, for low valence electron band fillings, the $\rho_{\mathrm{I}}(E)$ distribution has lower total energies. Under these same conditions, the $\rho_{\mathrm{II}}(E)$ distribution has lower electronic energy for higher band fillings. Similarly if μ_4 of $\rho_{\mathrm{I}}(E)$ is greater than the μ_4 of $\rho_{\mathrm{II}}(E)$ but where in addition the third moments of $\rho_{\mathrm{I}}(E)$ and $\rho_{\mathrm{II}}(E)$ are equal, then the I geometry has lower total energies at very low and very high electron band fillings while the II geometry is energetically more stable near the half-filled band. These findings are summarized in Fig. 2. In this figure we plot the difference in electronic energies between $\rho_{\mathrm{I}}(E)$ and $\rho_{\mathrm{II}}(E)$ as a function of electron band filling.

When both μ_3 and μ_4 play a role in the difference in energy, the energy difference curve is a composite of the
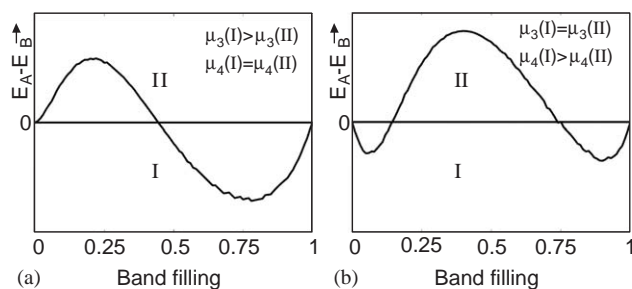
Fig. 2. The role of μ_3 and μ_4 in the relative stability of two hypothetical structures, I and II, as a function of fractional band filling.
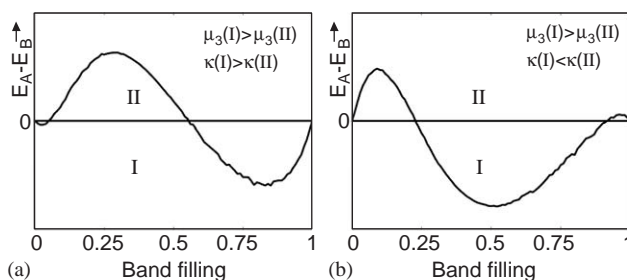

Fig. 3. The role of kurtosis in the relative stability of two hypothetical structures, I and II, as a function of fractional band filling. Notice that in (a) structure II is most stable for most low band-fillings. The kurtosis affects the width and position of this region of structure II stability. For $\kappa(I) < \kappa(II)$, this region is made narrower and shifted to lower electron counts. For $\kappa(I) > \kappa(II)$, it is broader and shifted to higher electron counts.

two separate curves given in Fig. 2. Unfortunately though, one cannot just look at the differences of μ_3 and μ_4 for the I and II geometries and then take a linear combination of the curves in Fig. 2a and b. We can however take such a linear combination if we define a new variable, the kurtosis, κ, which for a densities of state in standard normal form, is

$$\kappa = \mu_4 - \mu_3^2 - 1. \tag{5}$$

As discussed in Appendix B, the kurtosis is a better measure of the "peakedness" of $\rho(r)$ than μ_4.

Here we note that if the I and II geometries have the same third moment, then the difference in κ equals the difference in the fourth moment. The curve shown in Fig. 2a, is therefore not just a curve plotting the difference in energy due to a difference in the fourth moments, it is also the difference in energy due to a difference in κ values.

Furthermore, unlike in the case of μ_3 and μ_4, one can take a linear combination of differences in μ_3 and kurtosis, the two separate curves of Fig. 2, and arrive at an approximate difference in energy. This linear combination is shown pictorially in Fig. 3. In this figure we consider the case where $\mu_3(I) > \mu_3(II)$. In Fig. 3a–b $\kappa(I)$ is, respectively, $>$ and $<$ than $\kappa(II)$.

For this paper, which deals with transition metal compounds with roughly one-quarter to a one-half of the s–p–d valence bands filled, we are particularly interested in the crossing between the I and II energies near the half-filled band. Where there is no difference in kurtosis, this crossing is at roughly a 0.4 filled band, an average of 7 valence electrons/atom. For systems where $\kappa(I) >$ or $< \kappa(II)$, this crossing shifts to, respectively higher and lower electron counts.

The functions on which Figs. 2 and 3 are based are as follows. We consider four terms in deriving these functions: μ_3 and κ, the upper valence band limit, E_u, and lower valence band limit, E_1. From these four values we generate an approximate expression for the electronic density of states. This definition requires determination of three terms c, d, and f where

$$E_u = -c + 2\sqrt{d}, \tag{6}$$

$$E_1 = -c - 2\sqrt{d}, \tag{7}$$

$$f = \frac{E + c + \sqrt{(E + c)^2 - 4d}}{2}. \tag{8}$$

We find an approximate density of states $\rho_{approx}(E)$,

$$\rho_{approx}(E) = Im\left\{ \frac{1}{E - \frac{1}{E - \mu_3 - \frac{\kappa}{E + c - f}}} \right\}. \tag{9}$$

2.5. 3-rings, 4-rings and bond angles

The moment μ_3 and κ are important, not just because they determine the energetics of the system, but also because it is possible to relate these terms to specific bonding patterns in the given structures. This is so as

$$\mu_n = Tr(H^n) = \sum_{i_1, \ldots, i_n} H_{i_1 i_2} H_{i_2 i_3} \ldots H_{i_{n-1} i_n} H_{i_n i_1}, \tag{10}$$

where Tr is the trace and H_{ij} refers to a Hamiltonian matrix element. The above equation tells us that terms composed of three and four Hamiltonian matrix elements directly affect μ_3 and μ_4. Triangles and squares of bonded atoms (which we call 3- and 4-rings) are important in these two moments. Also important in the fourth moment are bond angles [37,42]. Recalling Eq. (5), 3- and 4-rings also prove important in the value of κ.

In this paper, we will use this connection to explain the differences in energy between the icosahedral Cr_3Si phase and the other closest packed phases. Through the intermediary of curves such as those shown in Figs. 2 and 3, we will be able to account for the difference in energy between icosahedral and closest-packed structures just by counting the number and types of 3- and 4-rings.

2.6. LDA-DFT calculations

For comparison with our tight-binding calculations with the μ_2-method, the electronic energies AB_3 were

calculated also using ab initio theory. Here, the $TaIr_3$ was optimized in each of the AB_3 structure types discussed in this paper using LDA-DFT via the VASP package [43–46]. The cell volumes, were first optimized using the conjugate-gradient algorithm available in the package, followed by relaxation of the atomic positions. All calculations were carried out using $15 \times 15 \times 15$ k-point meshes generated with the Monkhorst–Pack scheme [47]. The ultra-soft Vanderbilt pseudopotentials [48] which came with the package were used through out. Plane wave basis sets were used in the high precision mode with an energy cut-off of 250.0 eV.

3. Results

3.1. Experimentally observed structure map

Following the procedures outlined in the technical section, we found 35 experimentally observed, low temperature, atomically ordered, magnetically unordered AB_3 transition metal phases. Fifteen formed in the $AuCu_3$ structure type and 12 in Cr_3Si type. In addition there were 11 phases which formed in one of the four remaining structure types: $SnNi_3$, $TiAl_3$, $TiCu_3$, and $TiNi_3$.

Five of the six structure types mentioned above correspond to closest packing arrangements of the atoms. $AuCu_3$ and $TiAl_3$ are ordered versions of the face-centered cubic (fcc) closest packing. Their structures are illustrated in Fig. 1. $AuCu_3$ is the simplest possible ordered fcc structure. Atoms on the cubic cell corner are of one atom type (A), while atoms on the cubic cell faces are of the other atom type (B). The $TiAl_3$ structure is double the cell size of the $AuCu_3$ structure and is of tetragonal symmetry.

The $SnNi_3$ and $TiCu_3$ structures are ordered variants of the hexagonal closest packing (hcp) structure (Fig. 1). $SnNi_3$ is of hexagonal symmetry while $TiCu_3$ is orthorhombic. Finally the $TiNi_3$ structure is yet another variant of the closest packing structure, the double hexagonal closest packing structure (dhcp). Textbooks [49] refer to fcc and hcp as, respectively, containing ABCABC (each letter different from the two preceding letters) and ABABAB (each letter the same as the letters two places away) packing. In this notation, dhcp is an ABACABAC packing. As reflection on these latter letters shows, the dhcp packing is intermediate between the fcc and hcp packings. The $TiNi_3$ variant of the dhcp packing is also illustrated in Fig. 1.

Unlike the other structures, Cr_3Si is not an ordered variant of a closest packing. It has a body-centered cubic cell. The minority atomic compound, A (or Si), sits on the cubic cell corners and body centers, while the majority component, B (or Cr) sits in pairs along each face. Its structure is illustrated in Fig. 1. As Fig. 1 shows,

the majority atom, B, forms an icosahedron around the minority A atom.

A number of cubic structures based on icosahedral packings are known [50]. In all these cases a crystallographic point group of T symmetry (T is a subgroup of both the icosahedral I_h and octahedral O_h groups) can be found. This T point group aligns the three cubic unit cell axes with the icosahedra. As a result the unit cell axes become 3-fold rotation axes of icosahedra. The Cr_3Si structure is the simplest member of this family.

Two questions arise from the above-structural description. First, why sometimes are closest packed structures adopted, while in other cases icosahedral packing (as found in Cr_3Si) are adopted? Second, what factors cause one closest packed ordered structure to be adopted for one phase and another structure type to be adopted for another phase? The use of two-dimensional structure maps helps answer these questions. In such a structure map, we reduce the AB_3 composition to two quantifiable parameters and then plot the structure types as a function of these parameters. In this paper we seek parameters which not only cluster phases with equivalent structure types together on the structure map, but also we look for parameters which can be directly applied in electronic structure calculations. The two parameters we choose here are the average number of valence electrons per atom (electrons/atom) and the difference in energy of the respective atomic d-orbitals (ΔH_{ii}).

We apply these parameters to the known 35 phases. The results are shown in Fig. 4. As can be seen in this figure, the icosahedral Cr_3Si structure is adopted for systems which are markedly chemically different than
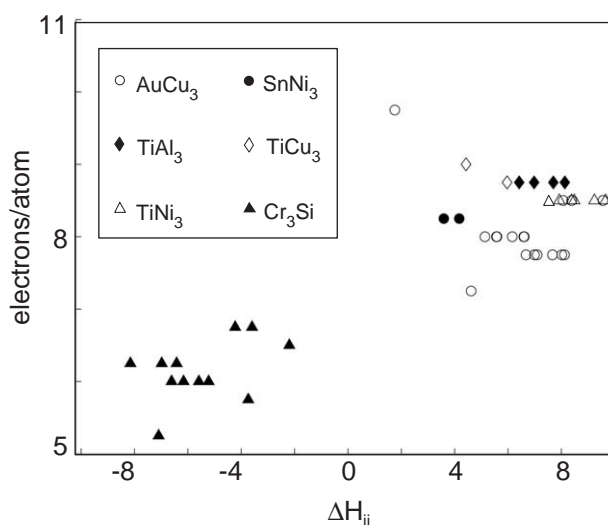

Fig. 4. Structure map for the known 35 atomically ordered, magnetically unordered AB_3 compounds. Good separation between the close-packed structures ($AuCu_3$, $SnNi_3$, $TiAl_3$, $TiCu_3$, $TiNi_3$) from the icosahedral Cr_3Si type is found for the parameters valences electrons/atom and ΔH_{ii}.

the closest packing structures. The Cr_3Si structure is adopted for systems with 5–7 electrons/atom where the minority component, A, is significantly more electronegative than the majority component, B ($-8 < \Delta H_{ii} < -2$ eV). By contrast the closest packing structures are found for systems with 7–10 electrons/atom and where the A component is more electropositive than the B component ($2 < \Delta H_{ii} < 10$ eV).

As Fig. 4 shows, these two parameters also allow us to differentiate between the different closest packing structures. The $AuCu_3$ structure is adopted in two regions: the first region is where ΔH_{ii} has a value near zero; the second region is where $4 < \Delta H_{ii} < 9$ eV and there are 8.5 or less electrons/atom. In the latter region, as the number of valence electrons increases beyond eight electrons/atom, first the $SnNi_3$, then the $TiNi_3$, and, finally, at 8.75 electrons/atom, the $TiAl_3$ and $TiCu_3$ structures are adopted.

As the above shows, the two parameters, electrons/atom and ΔH_{ii} may be used to differentiate between the six structure types. But such review of experimental data by itself does not allow one to delineate the actual factors responsible for the stability of a given phase. To identify such factors one must turn to the energies of different structures.

3.2. Theoretically derived structure map

We center our theoretical analysis on semi-empirical band calculations. Such calculations, unlike more complex ab initio ones, allow the reduction of a full band calculation to just a few simple parameters. In the semi-empirical tight-binding calculations used in this paper, the most pertinent such parameters are the difference in energy of the constituent atomic orbitals (ΔH_{ii}) and the total number of valence electrons. The first corresponds to the difference in electronegativity between the atoms, while the second leads to the average number of valence electrons per atom (electrons/atom).

In Fig. 5 we show the results of tight-binding calculations as a function of these parameters. Fig. 5a–c plots the difference in energy between the six structure types as a function of electrons/atom for, respectively, $\Delta H_{ii} = -10, 0$, and 10 eV. Recalling the definition of ΔH_{ii} we note that for AB_3 compounds when ΔH_{ii} is negative, the A atom is more electronegative.

The differences in energy curves plotted in Fig. 5 are given as a function of electrons/atom. Plotted is the difference in energy, ΔE, between a given structure and the $AuCu_3$ structure type for given values of ΔH_{ii} and electrons/atom. The convention is that when ΔE is negative, the $AuCu_3$ structure type is energetically preferred. The differences of energy of all six structures are plotted using the same convention. This allows for a simple interpretation of the graphs. At a given electron
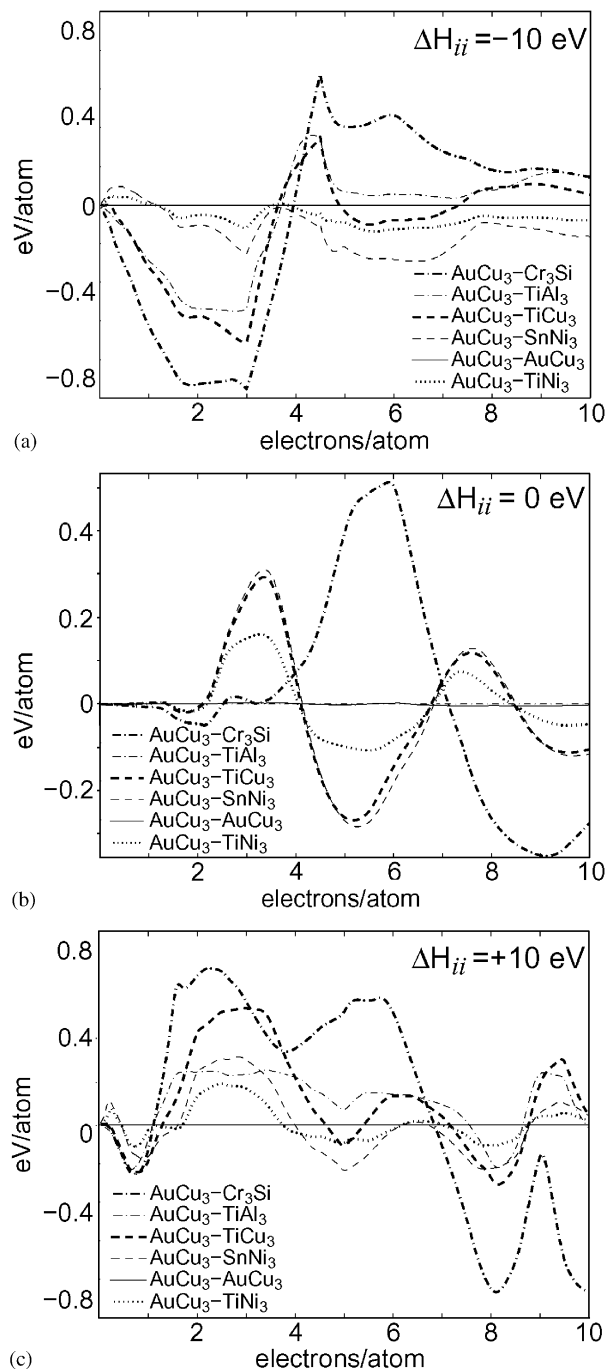

Fig. 5. Relative tight-binding energies for the $AuCu_3$, Cr_3Si, $TiAl_3$, $TiCu_3$, $SnNi_3$, $TiNi_3$ structure types as a function of valence electron count per atom at (a) $\Delta H_{ii} = -10$ eV, (b) $\Delta H_{ii} = 0$ eV, and (c) $\Delta H_{ii} = +10$ eV. The graphs read such that the highest curve at a given electron count is the most stable structure. The calculations include interactions for all atomic contacts within 10 Å. All AB_3 compounds discussed in this paper fall within the 5.25–9.75 on the electrons/atom axis.

count, the most energetically preferred structure is the structure whose ΔE curve is most positive.

As Fig. 5a shows, for $\Delta H_{ii} = -10$ eV, the $AuCu_3$ curve is most positive between approximately 1.5 and 3.5 electrons/atom. This structure is therefore most

favored for this range of electrons/atom. In the same way, the Cr_3Si structure is favored from four to 9.5 electrons/atom. We can compare these results with experiment. Experimentally, the only observed compounds with a negative value of ΔH_{ii} are compounds with electrons/atom values ranging from 5 to 7 (see Fig. 4). According to the results of Fig. 4a, we therefore anticipate that the observed structures with $\Delta H_{ii} < 0$ should all have the Cr_3Si structure type; this is indeed observed.

By contrast, as Fig. 5c shows, for $\Delta H_{ii} = +10\,eV$, the Cr_3Si structure is preferred from 1 to 6.5 electrons/atom (with the exception of a small zone of stability for the $TiCu_3$ structure near three electrons/atom), while a mixture of closest packed structures are preferred between 7.5 to 10 electrons/atoms. This latter region is quite complex. In particular, the $AuCu_3$ structure is preferred from 7.5 to 8.6, $TiAl_3$ from 8.7 to 9.1 and $TiCu_3$ from 9.1 to 10 electrons/atom. Also, the $TiNi_3$ structure is close in energy to the most preferred structure at 8.5 electrons/atom.

Again we can compare these theoretical results with the experimental structure map. As Fig. 4 shows, for $\Delta H_{ii} > 4\,eV$, $AuCu_3$ is found from 7.75 to 8.5 electrons/atom, $TiNi_3$ at 8.5 electrons/atom, $TiAl_3$ at 8.75 electrons/atom and $TiCu_3$ at 8.75 and 9.0 electrons/atom. These experimental zones of stability correspond to the results of the band calculations cited in the paragraph above.

The indication is therefore that there may be good agreement between theory and experiment. In order to test this hypothesis we therefore calculated differences of energies between the six structures for ΔH_{ii} values of $10, 8, 6, \ldots, -8$, and $-10\,eVs$. We then interpolated between these results to deduce which of the six structures was lowest in energy for given values of ΔH_{ii} and electrons/atom.

We plot the results of these calculations in Fig. 6. To allow the ready comparison of theory to experiment, we plot Fig. 5 on the same scale as that used in our experimental structure maps. We plot, at given values of both ΔH_{ii} and electrons/atom, which of the six structures are either most stable or within $0.05\,eV/atom$ of the most stable structure. For ease of comparison, also placed in Fig. 6 are the actual phases observed. As this figure shows, there is a good correlation between observed structure types and the structure predicted by our tight-binding band calculations. In all cases the observed structures are found within the zone predicted by the quantum mechanical calculations or are just outside the predicted stability zone.

Some stability zones are of particular interest. Among these is the thin $TiNi_3$ stability zone, found at $6 < \Delta H_{ii} < 10\,eV$ for 8.5 electrons/atom (Fig. 6c). This region is between broader regions for, on the one hand, the fcc structure $AuCu_3$ (found from 7.5 to 8.5 electrons/
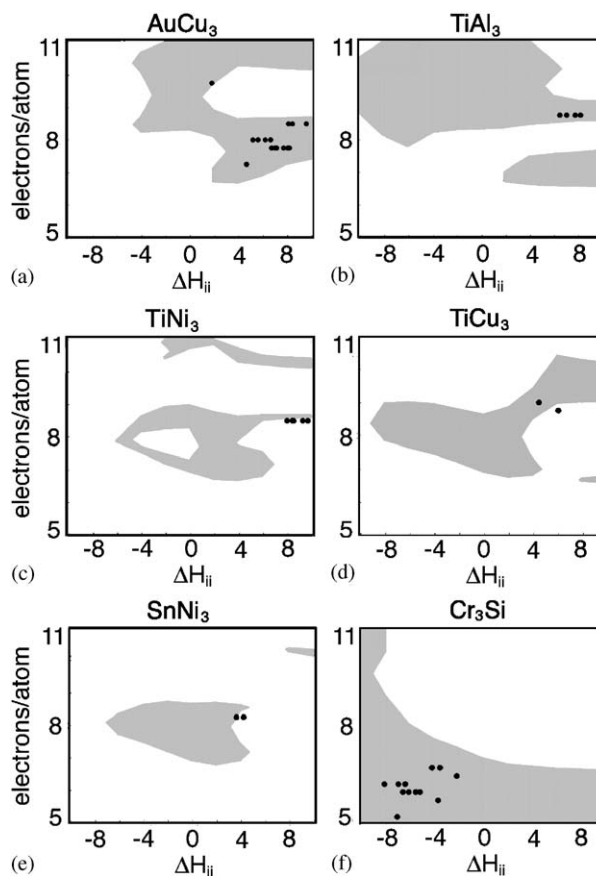

Fig. 6. Tight-binding regions of stability with respect to band filling and ΔH_{ii} for the (a) $AuCu_3$, (b) $TiAl_3$, (c) $TiNi_3$, (d) $TiCu_3$, (e) $SnNi_3$, and (f) Cr_3Si. The shaded regions correspond to electron counts and ΔH_{ii} values for which the respective structure type is most stable or within $0.05\,eV$ of the most stable one. The experimentally observed occurrences of each structure type are plotted as dots for comparison.

atom) and, on the other hand, the hcp $TiCu_3$ structure (found from 8.6 to 9.5 electrons/atom). As mentioned earlier, the $TiNi_3$ is a dhcp closest packed structure, a structure intermediate between the fcc and hcp types. The energetic results therefore follow the structural systematics.

A second area of interest is those regions on Figs. 5 and 6 where $\Delta H_{ii} \approx 0$. As Fig. 6 shows, in this region, the $TiAl_3$ and $AuCu_3$ stability zones closely resemble one another. This is so as both $TiAl_3$ and $AuCu_3$ are different ordered arrangements of the same fcc closest packing. At $\Delta H_{ii} = 0$ there is no difference between A and B atoms and therefore there is no difference in energy between these two structures. Similarly, as $TiCu_3$ and $SnNi_3$ are both ordered hcp types, their energies are also both the same when $\Delta H_{ii} \approx 0$.

Away from $\Delta H_{ii} = 0$, the differences between $AuCu_3$ and $TiAl_3$ or $TiCu_3$ and $SnNi_3$ becomes more evident. For high ΔH_{ii} values, both $AuCu_3$ and $TiCu_3$ have larger regions of stability than, respectively, $TiAl_3$ or $SnNi_3$. This finding is confirmed experimentally. $AuCu_3$

is much more prevalent for $\Delta H_{ii} > 8$ eV. Similarly $TiCu_3$ is observed for ΔH_{ii} values for 4.4–6.0 eV while $SnNi_3$ is observed at lower values ranging from 3.6 to 4.2 eV.

3.3. Stability calculations for $TaIr_3$ using ab initio theory

To calibrate the accuracy of the above tight-binding calculations, we compare them to those from a higher-level ab initio theory, LDA-DFT. As such DFT calculations, unlike tight-binding calculations, are applied to actual chemical rather than model systems, we choose an actual compound on which to perform the calculations. We consider here $TaIr_3$. We choose this compound as the two elements involved have a reasonably large difference in electronegativity, and as both elements are from the same row in the periodic table, the elements are related to one another in the size of their atomic orbitals. $TaIr_3$ therefore tests the electronic variables which are the principal concern of this paper, electron count and ΔH_{ii}, rather than steric variables such as orbital size.

In Table 3, we compare the relative energies of the $TaIr_3$ compound between the six different structure types: $AuCu_3$, $SnNi_3$, $TiNi_3$, $TiAl_3$, $TiCu_3$, and Cr_3Si. Also listed in Table 3 are the relative tight-binding energies for an average of eight valence electrons/atom and with $\Delta H_{ii} = 6$ eV (the electron count and the ΔH_{ii} value of $TaIr_3$). As this table shows, the μ_2-Hückel and LDA-DFT calculations give qualitatively similar results. Both types of calculation place the energies of the six structures in the same order: $AuCu_3$ is lowest in energy, followed sequentially by $SnNi_3$, $TiNi_3$, $TiAl_3$, $TiCu_3$, and finally at the highest energy, Cr_3Si. (In agreement with these calculations, $TaIr_3$ is found in the $AuCu_3$ structure type). The calculational results suggest that μ_2-Hückel theory correctly assesses not just the lowest energy structure (as we inferred from the previous reported comparisons between theory and experiment) but differences in energy between higher energy geometries as well. Numerically though, μ_2-Hückel energies suffer from a scaling error. Energy differences are overestimated, and this overestimation appears to vary as a function of the absolute difference in energy to the ground state structure.

These results lend further credence to the qualitative accuracy of the μ_2 tight-binding calculation. This is important. The numerical agreement between μ_2-Hückel

and LDA-DFT energies allow us to more readily believe the structure-energy relation derived from μ_2-Hückel theory. In particular, it will support the arguments based on the importance of 3- and 4-member rings of bonded atoms.

3.4. Cr_3Si vs. $AuCu_3$

In this section, we use tight-binding theory to delve deeper into the structural reasons behind the features observed in the structure maps, specifically why the Cr_3Si structure is preferred for some electron counts and closest packed structures for other electron counts. In this analysis, we choose just one closest packed structure, that of $AuCu_3$, but as our discussion will show, many of the same effects discussed here for the $AuCu_3$ structure will prove pertinent to all closest packed structures.

Although the final picture is much simpler, the analysis is rather involved. We include this section for specially readers who have an interest in how the structure and energy are bridged via the moments method. Readers whose interests in tight-binding calculations are more cursory may go directly to the summary of this analysis (Section 3.4.2) without missing the thrust of our arguments.

In essence, we will follow the difference in energy curve between the $AuCu_3$ and Cr_3Si structures as we turn sequentially from the full band calculation, to a bond calculation involving first nearest-neighbor bonds only, then to the third and fourth moments of the nearest-neighbor bond calculation, and finally to the number of triangles and squares of bonded atoms in the two structure types. We will follow this chain of calculations for a range of ΔH_{ii} values. When the analysis is finished, we will have defined a set structural factors responsible for the energy differences between the icosahedral Cr_3Si and closest packed $AuCu_3$ structures.

We begin with the full band calculations. Earlier, we showed the difference in energy between the $AuCu_3$ vs. the Cr_3Si structure for $\Delta H_{ii} = 10$, 0, and -10 eV ($\Delta H_{ii} = H_{ii}(A) - H_{ii}(B)$, where A and B refer to the two elemental components of the AB_3 compound) as the dash-dotted lines in Fig. 5. For $\Delta H_{ii} = 10$ eV there were two broad peaks in which the Cr_3Si structure is preferred (centered roughly at 2 and 5 electrons/atom), while from 7 to 10 electrons/atom the $AuCu_3$ structure is energetically favored.

The $\Delta H_{ii} = 0$ eV curve bears similarities to the preceding one. One notable difference is that the first peak favoring the Cr_3Si structure centered at two electrons/atom has disappeared. For $\Delta H_{ii} = 0$, neither structure type is particularly favored from 1–4 electrons/atom. A second difference is that the amount by which the $AuCu_3$ structure is favored from 7 to 10 electrons is

Table 3
Calculated energies of $TaIr_3$ in common AB_3 structure types

	$AuCu_3$	$SnNi_3$	$TiNi_3$	$TiAl_3$	$TiCu_3$	Cr_3Si
LDA-DFT[a]	0.00 eV	0.006	0.008	0.155	0.182	0.630
μ_2-Hückel[a]	0.00 eV	0.032	0.079	0.184	0.324	0.869

[a] Per atom, relative to $TaIr_3$ in the $AuCu_3$ structure type.

roughly halved. For example, the maximum amount by which the $AuCu_3$ structure is favored has reduced from about 0.87 eV/atom to only 0.39 eV/atom.

The trends observed in going from $\Delta H_{ii} = 10$ to 0 eV continues in going from 0 to -10 eV. At -10 eV, between 1 and 4 electrons/atom, the $AuCu_3$ structure is now the preferred structure, while from 7 to 10 electrons/atom the region of $AuCu_3$ stability has disappeared and now slightly favors the Cr_3Si structure. However, the peak of Cr_3Si stability centered at five electrons/atom remains at approximately the same height.

The above results include all atomic interactions between atoms less than 10 Å apart. These results therefore combine the energetic effects due to atoms which are bonded to one another, and those atoms which are too far from one another to be bonded in a classical manner. As we now seek the origin of energetic preferences, we differentiate between bonding and non-bonding contacts. We recalculate the difference in energies between the $AuCu_3$ and Cr_3Si structure types setting all off-diagonal Hamiltonian matrix elements between atoms greater than 3.0 Å apart to be formally zero. The results of these calculations are shown in Fig. 7.

There are marked similarities between the $AuCu_3$–Cr_3Si energy curves of Figs. 5 and 7. In both cases, for $\Delta H_{ii} = 10$ eV, the Cr_3Si structure is preferred from zero to roughly 7 electrons, but the $AuCu_3$ structure is favored from 7 to 10 electrons. The initial zone of Cr_3Si stability centered at two electrons/atom is largely lost in going from $\Delta H_{ii} = 10$ to 0 eV. Furthermore, in going from 10 to 0 eV, the zone of $AuCu_3$ stability between 7 and 10 electrons/atom is approximately halved. Finally, for $\Delta H_{ii} = -10$ eV, $AuCu_3$ is
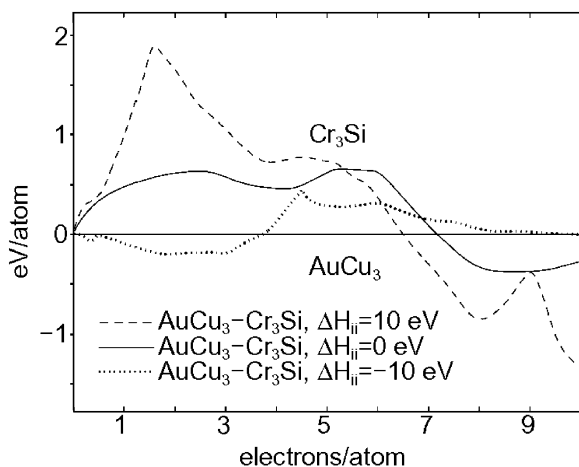
the more stable between 1 and 4 electrons/atom, while Cr_3Si is the more stable between 7 and 10 electrons/atom. The curves of Figs. 5 and 7 are sufficiently similar that we conclude it is near neighbor interactions which are primarily responsible for the main energetic differences between the two structure types.

We now consider the moments of the $AuCu_3$ and Cr_3Si densities of state, see the technical section and Appendix A. Our interest here is the energetic role the different moments play in the densities of states. For those unfamiliar with moments analyses, we note that as the zeroth, first and second moments are formally equal in our tight-binding calculation, the leading moments describing the differences in the densities of states are the third and fourth moments.

In Fig. 8 we use Eqs. (6)–(9) and calculate the difference in energy between the $AuCu_3$ and Cr_3Si structures using only the third and fourth moments, and the lower and upper limits of the valence energy bands, E_l and E_u (we continue to set off-diagonal interactions between atoms further than 3.0 Å apart to be formally zero). This is a major approximation. Comparing the results of Figs. 7 and 8, we find the latter are highly simplified.

However, the main trends previously discussed for Fig. 7 are preserved in Fig. 8. In particular for $\Delta H_{ii} = 10$, at low electron counts (from 0 to 6 electrons/atom), the Cr_3Si structure is preferred, while $AuCu_3$ is favored at higher electron counts. The stability of the Cr_3Si structure at low electron counts (from 0 to 4 electrons/atom) is roughly halved in going from $\Delta H_{ii} = 10$ to 0 eV. These trends continue in the -10 eV case. Here, at the lowest electron counts, the $AuCu_3$ structure is preferred, while from 7 to 10 electrons/atom the Cr_3Si structure is preferred. We conclude the main differences of energy between the $AuCu_3$ and Cr_3Si structures can be understood in terms of four variables: μ_3, μ_4, E_l and E_u. Of these four, the first two prove to be of greatest importance.

In Table 4, we list the third moment, fourth moment and the kurtosis for the $AuCu_3$ and Cr_3Si structures for $\Delta H_{ii} = 10$, 0 and -10 eV in standard normal form. In each case the Cr_3Si structure has a more negative third moment. But for -10 eV the Cr_3Si fourth moment (as well as kurtosis) is smaller than that of $AuCu_3$ while the fourth moment is larger for 10 and 0 eV. This is precisely the case we discussed in Fig. 4. The third moment of one structure is more negative but there is variation in which structure has the lower fourth moment and the lower kurtosis.

As we noted in our earlier discussion, the effect of alternation in the fourth moment is to shift the crossings from one structure type to the other structure type. In the absence of any fourth moment contribution, there is a crossing at the 0.4 band filled level (i.e., 7 electrons/atom) this crossing shifts to a lower or higher electron
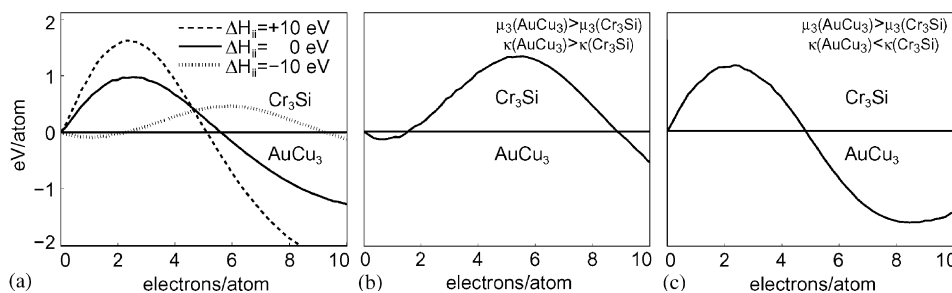

Fig. 7. Relative tight-binding energies for the $AuCu_3$ and Cr_3Si structure types as a function of valence electron count per atom at $\Delta H_{ii} = -10$ eV, $\Delta H_{ii} = 0$ eV, and $\Delta H_{ii} = +10$ eV. The calculations exclude interactions for all atomic contacts longer than 3.00 Å. See caption to Fig. 5 for a description of the graph conventions.

Fig. 8. Relative energies of AuCu$_3$ and Cr$_3$Si structures (a) based solely on μ_3, κ, E_1, E_u and near-neighbor atomic contacts ($\leqslant 3.0$ Å). Plots are given for $\Delta H_{ii} = +10$, 0 eV, and -10 eV; (b) with $\mu_3(\text{AuCu}_3) > \mu_3(\text{Cr}_3\text{Si})$ *and* $\kappa(\text{AuCu}_3) > \kappa(\text{Cr}_3\text{Si})$; (c) with $\mu_3(\text{AuCu}_3) > \mu_3(\text{Cr}_3\text{Si})$ *but* $\kappa(\text{AuCu}_3) < \kappa(\text{Cr}_3\text{Si})$. Note the similarity between the curves for (a) $\Delta H_{ii} = -10$ eV and (b). Note also the similarities between (a) $\Delta H_{ii} = +10$ or 0 eV and (c). In (b) and (c) the same difference in μ_3 was used.

Table 4
Adjusted moments of $\rho_{\text{Cr}_3\text{Si}}$ and ρ_{AuCu_3}[a]

	$\Delta H_{ii} = +10$ eV		$\Delta H_{ii} = 0$ eV		$\Delta H_{ii} = -10$ eV	
	AuCu$_3$	Cr$_3$Si	AuCu$_3$	Cr$_3$Si	AuCu$_3$	Cr$_3$Si
μ_0	1.00	1.00	1.00	1.00	1.00	1.00
μ_1	0.00	0.00	0.00	0.00	0.00	0.00
μ_2	1.00	1.00	1.00	1.00	1.00	1.00
μ_3	−0.718	−0.896	−0.544	−0.689	−0.518	−0.546
μ_4	3.70	4.04	3.73	3.97	2.89	2.80
κ	2.19	2.24	2.43	2.49	1.62	1.50

[a]Scaled such that $\mu_0 = 1.00$, $\mu_1 = 0$ and $\mu_2 = 1.00$.

Table 5
Decomposition of the normalized, standardized μ_3 of $\rho_{\text{Cr}_3\text{Si}}$ and ρ_{AuCu_3} into walks

	$\Delta H_{ii} = +10$ eV		$\Delta H_{ii} = -10$ eV	
	AuCu$_3$	Cr$_3$Si	AuCu$_3$	Cr$_3$Si
3-atom paths	−0.95	−1.13	−0.37	−0.40
2-atom paths	−2.13	−2.13	−1.54	−1.54
1-atom paths	−1.24	−1.24	−1.79	−1.79
Other terms in μ_3[a]	+3.60	+3.60	+3.18	+3.18
Total μ_3	−0.72	−0.90	−0.52	−0.55

[a]Last and penultimate terms in Eq. (15).

count depending on the differences in the kurtosis. In Fig. 8b–c, we redraw the results of Fig. 4, where we normalize the band filling to the s–p–d valence band. As we are interested in only transition elements, we consider electron counts ranging from completely empty to slightly more than half-filled (i.e., with 10 d-electrons or $\frac{10}{18}$ of the band filled).

A comparison of Figs. 8a–c shows that the evolution in the difference if energy between AuCu$_3$ and Cr$_3$Si can be attributed to changes in the third and fourth moments of these two structures. For $\Delta H_{ii} = 10$ and 0 eV, the Cr$_3$Si structure has a more negative third moment and a more positive kurtosis. For $\Delta H_{ii} = -10$ eV, Cr$_3$Si has the more negative third moment, *but* AuCu$_3$ has the more positive kurtosis. It is the tension between the third moment and the kurtosis which is responsible for the shifts in structural stability.

3.4.1. Structure-dependent energy differences for Cr$_3$Si and AuCu$_3$

In the previous section, we saw that the principal terms controlling the differences in energy between the Cr$_3$Si and AuCu$_3$ structure types were μ_3 and μ_4. We found for all values of ΔH_{ii} that Cr$_3$Si has the greater μ_3 value, but while at $\Delta H_{ii} = 10$ or 0 eV, Cr$_3$Si has the greater μ_4 (and κ) value, that at $\Delta H_{ii} = -10$ eV, AuCu$_3$ structure has the greater μ_4 (and κ) value.

We now examine the specific bonding motifs responsible for these differences. We turn first to μ_3. In Table 5, we show the value of μ_3 for the two structure types for the two limiting values of ΔH_{ii}, -10 and $+10$ eV. We further decompose the μ_3 term into four parts, those paths of length 3 involving 1, 2 or 3 different atoms and those terms which come about from normalization (see Appendix A, Eq. (15)). As this table shows, only for paths which involve three different atoms, does the value of μ_3 differ much between the two structure types. Important paths involving three different atoms are the 3-rings in the system, i.e., triangles of atoms which are all bonded to one another. To account for the difference in μ_3 we must therefore account for the different number of 3-rings in the two structures.

For high-coordination intermetallic systems such as Cr$_3$Si and AuCu$_3$, enumeration of 3-rings is most efficiently carried out by considering the different coordination polyhedra. The coordination polyhedra of both the AuCu$_3$ and Cr$_3$Si structures are shown in Fig. 9. In AuCu$_3$, there are two different polyhedra, one centered on the Au atom and the second centered on a Cu atom. As Fig. 9 shows, both these polyhedra are 12-coordinate cubooctahedra. In the case of Cr$_3$Si, the Si atoms lie in the center of 12-coordinate icosahedra while the Cr atoms lie in the center of 14-coordinate Frank–Kasper polyhedra (this last polyhedron is a
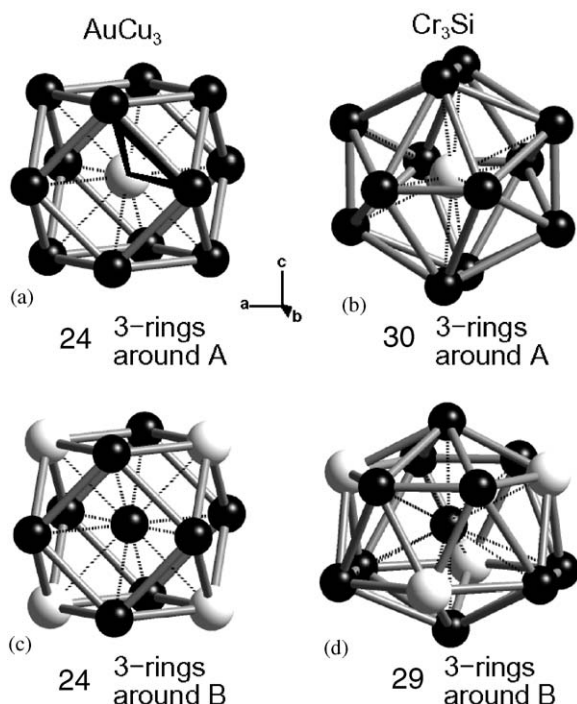
Fig. 9. Near-neighbor coordination polyhedra for the AB_3 structure types $AuCu_3$ and Cr_3Si. (a) Au-centered coordination polyhedra in the $AuCu_3$ structure. (b) Si-centered polyhedra in the Cr_3Si structure. (c) Cu-centered polyhedra in $AuCu_3$ structure. (d) Cr-centered polyhedra in the Cr_3Si structure. Au and Si atoms: white spheres, Cu and Cr atoms: black spheres. The numbers of 3-rings passing through the polyhedral center are given. In (a) one of these 3-rings has been highlighted. In (d) this number has been normalized, see text.

Table 6
Decomposition of the normalized, standardized μ_4 of ρ_{Cr_3Si} and ρ_{AuCu_3} into walks

	$\Delta H_{ii} = +10\,eV$		$\Delta H_{ii} = -10\,eV$	
	$AuCu_3$	Cr_3Si	$AuCu_3$	Cr_3Si
4-rings	1.03	1.39	0.43	0.38
Angles	2.16	2.16	1.22	1.19
Other terms in μ_4	0.51	0.49	1.24	1.22
Total μ_4	3.71	4.04	2.89	2.80

$AuCu_3$ structure has the greatest μ_4. It is this change in the fourth moment which is responsible for the different differences of energy curve seen in Fig. 8.

To understand the evolution in the fourth moment, we decompose it into three parts, those involving, respectively 4-rings of atoms, bond angles and finally all other terms involving three or fewer different atoms. As Table 6 shows, while all three of the above terms play a significant role in the fourth moment, it is the change in the contributions from the 4-rings which play the most significant role in going from $\Delta H_{ii} = +10$ to $-10\,eV$. Thus for $+10\,eV$ the difference in μ_4 between the two structures is 0.33, while the difference in 4-rings is 0.36, while at $-10\,eV$, the difference in μ_4 is -0.09, while the difference in 4-rings is -0.05.

We can account for the changes in 4-rings if we decompose all 4-rings into the three principal types, those involving alternating $ABAB$ atoms, those involving only one A but three B atoms, and those involving only B atoms (there are only these three types as there are no A–A bonds in either $AuCu_3$ or Cr_3Si). In Fig. 10, we show the first coordination polyhedron centered on an A atom together with either A or B atoms from the second coordination polyhedra. From these pictures we can directly enumerate all alternating $ABAB$ and $ABBB$ 4-rings passing through the central A atom. As this figure shows, there are 72 and 48 $ABAB$ 4-rings for, respectively, $AuCu_3$ and Cr_3Si. But, as this figure also shows there are 192 and 240 $ABBB$ 4-rings for, respectively, these same two structures. Thus $AuCu_3$ has 50% more $ABAB$ 4-rings but 20% fewer $ABBB$ 4-rings than Cr_3Si.

This difference in 4-rings is seen in the actual contributions of each type of 4-ring to the overall fourth moment. In Fig. 11, we show the contribution to the total fourth moment from separately the $ABAB$, $ABBB$ and $BBBB$ 4-ring motifs for $\Delta H_{ii} = +10$ to $-10\,eV$. As this table shows, the contributions of the $ABAB$ and $ABBB$ parts follows the different numbers of rings in the two structure types. Thus for both $\pm 10\,eV$ the $AuCu_3$ $ABAB$ and $ABBB$ terms are, respectively, 50% greater and 25–50% smaller than the Cr_3Si values.

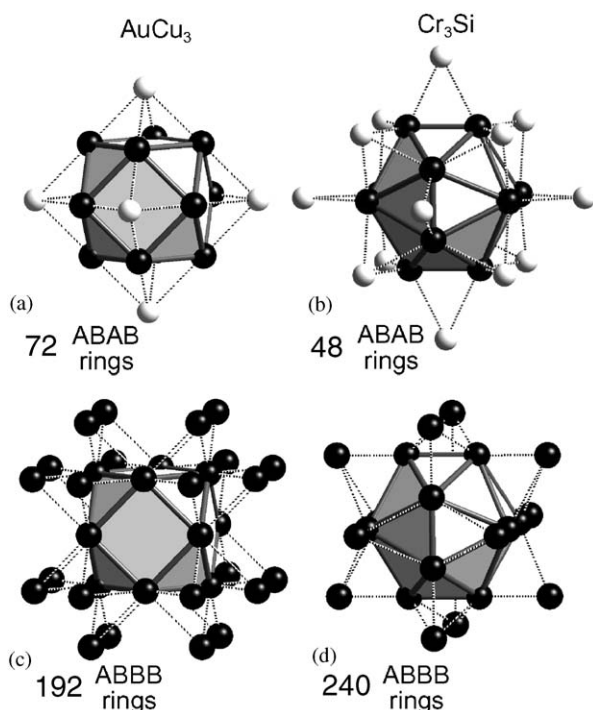Fig. 11 shows that the evolution in the fourth moment is caused by the relative importance of $ABAB$ and $ABBB$

hexagonal antiprism with both its hexagonal faces capped).

To enumerate the 3-rings, we count all 3-rings which pass through the central atom of the polyhedra. These numbers are tabulated in Fig. 9, adjacent to each of the coordination polyhedra. In the case of the 14-coordinate Frank–Kasper polyhedron, we further normalize this value to take into account the higher coordination number of the system. (As the goal here is to compare the 14-coordinate polyhedra to 12-coordinate polyhedra, second moment scaling gives in this case a normalization factor of $(12/14)^{\frac{3}{2}}$, see Appendix A.) As shown in Fig. 9, the two $AuCu_3$ coordination polyhedra have 24 3-rings, while the Cr_3Si polyhedra have 30 and 29 3-rings. There are therefore roughly 25% more 3-rings in the Cr_3Si structure than the $AuCu_3$ structure. It is therefore not surprising that the 3-ring contribution to μ_3 is roughly 10–20% larger in the former geometry, see Table 5.

We now turn to the geometrical factors responsible for differences in μ_4. In Table 6, we show the fourth moment for $\Delta H_{ii} = +10$ and $-10\,eV$. As noted previously, while for $\Delta H_{ii} = +10\,eV$ the Cr_3Si structure has the largest fourth moment, at $\Delta H_{ii} = -10\,eV$, the

Fig. 10. Second coordination shells around the Au and Si atoms in respectively the $AuCu_3$ and Cr_3Si structures. (a) Au-, (b) Si-, (c) Cu-, (d) Cr-atoms of the second coordination shell that bridge atoms of the first coordination polyhedra. Au and Si atoms: white, Cu and Cr atoms: black. The numbers of 4-rings passing through the central atom are given. As all first coordination polyhedra are 12-coordinate, no normalization is needed.

Fig. 11. Contributions to the fourth moment from 4-rings in AB_3 compounds in the $AuCu_3$ and Cr_3Si structure types. Contributions given in eV^4/atom ($9 \times \mu_4^0$), see Appendix A.

4-rings to the total 4-ring contribution of the fourth moment [51]. In particular for $\Delta H_{ii} = +10$ eV, the $ABBB$ 4-ring term dominates, while for -10 eV, the $ABAB$ term plays a slightly greater role. To account for the evolution in the fourth moment in going from $+10$ to -10 eV, we must explain why $ABBB$ 4-rings are most important at $+10$ eV but they are not as important at -10 eV.

The explanation for this effect lies in the Wolfsberg–Helmholtz approximation:

$$H_{ij} = \frac{K}{2}(H_{ii} + H_{jj})S_{ij}, \qquad (11)$$

where H_{ij}, H_{ii}, and S_{ij} are, respectively, the off-diagonal Hamiltonian matrix element, the on-site Coulombic integral and the overlap integral between the i and j atomic orbitals. For $\Delta H_{ii} = +10$ eV, the A and B atom d-orbitals have an H_{ii} values of, respectively, -6 and -16 eV, while for -10 eV they have values of, respectively, -16 and -6 eV. Thus in going from $\Delta H_{ii} = +10$ to -10 eV, while $H_{ii} + H_{jj}$ (and consequently H_{ij}) is constant for A–B bonds, the $H_{ii} + H_{jj}$ terms for B–B bonds become roughly three times weaker. It is this change in relative A–B and B–B H_{ij} terms which is responsible for the changes in the $ABBB$ vs. $ABAB$ 4-ring contributions, and consequently it is this change which is responsible for the different fourth moment effects at $\Delta H_{ii} = \pm 10$ eV.

3.4.2. Icosahedral Cr_3Si vs. closest-packed $AuCu_3$

In the previous sections, we have told an involved story. Within the context of tight-binding theory, we have found the factors responsible for the stability of the Cr_3Si and $AuCu_3$ structure types. The former structure is the simplest of all icosahedral phases, a family which extends to many remarkable intermetallic crystalline and quasi-crystalline structures, while the former is a fine example of an ordered closest packing. In view of the importance of both icosahedral and closest-packed structures, it may be useful to recapitulate the arguments previously presented, but in a form which seeks to emphasize chemical bonding principles.

As Fig. 4 and Table 1 show, the icosahedral Cr_3Si structure is stable for systems with negative ΔH_{ii} values and an average of 5–7 valence electron/atom. The closest-packed $AuCu_3$ structure is stable for positive ΔH_{ii} values and 7–10 electrons/atom. As Fig. 8 shows, these trends can be understood by considering the third and fourth moments for these two structures. The third moment term is responsible for the stability of the Cr_3Si structure from 5 to 7 electrons/atom for all values of ΔH_{ii}; the fourth moment term causes the stability region of the Cr_3Si structure to shift from 1–10 electrons/atom for $\Delta H_{ii} = -10$ eV to 0–6 electrons/atom for $\Delta H_{ii} = +10$ eV.

Thus the stability of the Cr_3Si structure from 5 to 7 electrons atom is due primarily to the third moment. The icosahedral Cr_3Si structure has more 3-rings, i.e., more triangles of bonded atoms and thus has a more negative third moment for all values of ΔH_{ii}. This larger number of triangles of bonded atoms is insufficient to account for the stability of the closest packed structures from 7 to 10 electrons/atom. Equally important here is the fourth moment contribution. In particular, for

positive values of ΔH_{ii}, B–B bonds are particularly strong. As in the Cr_3Si structure there are a greater number of $ABBB$ 4-rings involving such B–B bonds, the fourth moment of the Cr_3Si structure becomes particularly large. The Cr_3Si structure is therefore destabilized near the half filled band. Thus from 7–10 electrons per atom, values near the half-filled band (recall that the valence band has s, p, and d components and therefore can accommodate a total of 18 electrons/atom) the $AuCu_3$ structure is favored.

4. Conclusion

This has been a story with a number of parts. We have suggested that it is the electron count and the difference in electronegativity which are most responsible for the differences in structure for AB_3 binary transition metal alloys. We have shown that tight-binding theory with second moment scaling can be used to account for these differences in energy, and that this theory can be used to discern the factors responsible for the structures. Not surprisingly, we have found that triangles of bonded atoms plays a role in differentiating icosahedral phases from closest packed structures. Perhaps more surprisingly, in certain cases, the larger number of icosahedral structure 4-rings also plays a role.

We can compare these results to earlier calculations performed on Frank–Kasper vs. closest packed elemental and alloy structures [52]. In this earlier work, it was found that the Frank–Kasper phases, the χ- and σ-phases, were more stable at 6–7 valence electrons/atom, but that closest packings, fcc and hcp, were stable from 7–10 electrons/atom. These results are comparable with the Cr_3Si vs. $AuCu_3$ results presented in this paper. Taken together, they suggest Frank–Kasper phases and closest packings are stable at, respectively, 5–7 and 7–10 electrons/atom. Within this context it would be interesting to study the stability of transition metal Frank–Kasper AB_2 Laves compounds and the known comparative absence of transition metal AB_2 closest packed structures.

Appendix A. Normalized moments

It proves useful to transform a density of states, as derived from a tight-binding calculation, into one which is in standard normal form, i.e., one where the zeroth, first and second moments are, respectively one, zero, and one. This transformation is straightforward but as the equations are somewhat cumbersome it is useful to explicitly state them here. The transformation takes place in three steps. In the first step we normalize the density of states, i.e., we set the zeroth moment equal to one. We do so by dividing all moments by the initial value of the first moment. We call this set of normalized (but not standardized) moments, μ_n^0.

In the second step, we redefine the zero energy so that the first moment is explicitly zero itself. For the first few moments we find:

$$\mu_0' = 1, \tag{12}$$

$$\mu_1' = 0, \tag{13}$$

$$\mu_2' = \mu_2^0 - (\mu_1^0)^2, \tag{14}$$

$$\mu_3' = \mu_3^0 - 3\mu_2^0\mu_1^0 + 2(\mu_1^0)^3, \tag{15}$$

$$\mu_4' = \mu_4^0 - 4\mu_3^0\mu_1^0 + 6\mu_2^0(\mu_1^0)^2 - 3(\mu_1^0)^4. \tag{16}$$

In the third and final step, we redefine the energy scale so that the second moment is explicitly one:

$$\mu_n = \mu_n'(\mu_2')^{-n/2}. \tag{17}$$

The values μ_n so defined are in standard normal form, with μ_0, μ_1, and μ_2, respectively, equal to one, zero, and one.

Appendix B. Kurtosis

Kurtosis is a quantity which comes in importance just after the variance as a measure of a density of states. Its definition is understood by first considering the simplest of all density of states functions, those composed of a single delta function. For such a density of states, the variance is necessarily zero, where variance, σ^2, is defined as

$$\sigma^2 = \begin{vmatrix} \mu_0 & \mu_1 \\ \mu_1 & \mu_2 \end{vmatrix} = \mu_2\mu_0 - \mu_1^2. \tag{18}$$

We now turn to a density of states which consists of a double delta function. This distribution is illustrated in Fig. 12. Here the two delta functions are at positions x_1 and x_2 with areas of respectively α and β. In this example, $\mu_n = \alpha x_1^n + \beta x_2^n$. For such a double delta function we find the quantity, κ is exactly zero, where κ is

$$\kappa = \begin{vmatrix} \mu_0 & \mu_1 & \mu_2 \\ \mu_1 & \mu_2 & \mu_3 \\ \mu_2 & \mu_3 & \mu_4 \end{vmatrix}. \tag{19}$$
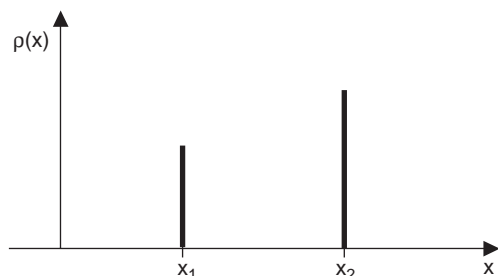
Fig. 12. A function with zero kurtosis: two delta functions, one at x_1, the other at x_2 with areas of, respectively, α and β. This construction is used in the text in determining an expression for kurtosis in terms of μ_0 through μ_4.

We summarize our above findings. For a density of states comprised of a single delta function, the variance, σ^2, is zero. For a density of states comprised of two delta functions $\kappa = 0$. Thus the variance is a measure of our ability to describe a density of states by a single energy value; κ is a measure of our ability to describe a density of states by a pair of values. This latter κ value is termed the kurtosis (though some further multiply the kurtosis by additional functions of the zeroth, first and second moment). The kurtosis is sometimes referred to as the peakedness of a density of states. In the case of a standard normal density of states, the kurtosis reduces to an especially simple form:

$$\kappa = \mu_4 - \mu_3^2 - 1. \tag{20}$$

References

[1] D.G. Pettifor, J. Phys.: Condens. Matter 15 (2003) V13–V16.
[2] A. Ker, E. Todorov, R. Rousseau, K. Uehara, F.-X. Lannuzel, J.S. Tse, Chem. Eur. J. 8 (2002) 2787–2798.
[3] M. Morinaga, H. Yukawa, Adv. Eng. Mater. 3 (2001) 381–385.
[4] A.M. Mills, A. Mar, J. Alloys Compds. 298 (2000) 82–92.
[5] H. Kleinke, B. Harbrecht, Z. Anorg. Allg. Chem. 626 (2000) 1851–1853.
[6] Y. Harada, M. Morinaga, J. Saito, Y. Takagi, J. Phys.: Condens. Matter 9 (1997) 8011–8030.
[7] S.I. Simak, U. Häußermann, I.A. Abrikosov, O. Eriksson, J.M. Wills, S. Lidin, B. Johansson, Phys. Rev. Lett. 79 (1997) 1333–1336.
[8] G.J. Miller, Eur. J. Inorg. Chem. (1998) 523–536.
[9] S. Lee, Annu. Rev. Phys. Chem. 47 (1996) 397–419.
[10] M.L. Fornasini, F. Merlo, J. Alloys Compds. 219 (1995) 63–68.
[11] R.E. Watson, J.W. Davenport, M. Weinert, L.H. Bennett, in: H. Brodowsky, H.-J. Schaller (Eds.), Thermochemistry of Alloys, Kluwer Academic Publishers, Netherlands, 1989.
[12] P. Villars, F. Hulliger, J. Less-Common Met. 132 (1987) 289–315.
[13] P. Villars, J. Less-Common Met. 99 (1984) 33–43.
[14] P. Villars, J. Less-Common Met. 102 (1984) 199–211.
[15] E. Mooser, W.B. Pearson, Acta Crystallogr. 12 (1959) 1015–1022.
[16] L. Pauling, The Nature of the Chemical Bond, third ed., Cornell University Press, Ithaca, NY, 1960.
[17] S. Raju, E. Mohandas, V.S. Raghunathan, Scripta. Mat. 34 (1996) 1785–1790.
[18] L.S. Smith, D.K. Tappin, M. Aindow, Scripta. Mat. 34 (1996) 227–234.
[19] M.A. Kassem, Scripta. Met. Mat. 32 (1995) 1191–1196.
[20] D.G. Pettifor, in: C.T. Liu, R.W. Cahn, G. Sauthoff (Eds.), Ordered Intermetallics—Physical Metallurgy and Mechanical Behaviour, Kluwer Academic Publishers, Netherlands, 1992.
[21] R.J. Kematick, C.E. Myers, Inorg. Chem. 31 (1992) 3568–3572.
[22] C.T. Liu, J.A. Horton, D.G. Pettifor, Mater. Res. Soc. Symp. Proc. 133 (1989) 37–43.
[23] D.G. Pettifor, Solid State Commun. 51 (1984) 31–34.
[24] U. Walzer, Phys. Status Solidi B 168 (1991) 397–412.
[25] S.B. Zhang, M.L. Cohen, Phys. Rev. B 39 (1989) 1077–1080.
[26] S.B. Zhang, M.L. Cohen, J.C. Phillips, Phys. Rev. B 36 (1987) 5861–5867.
[27] J.K. Burdett, G.D. Price, S.L. Price, Phys. Rev. B 24 (1981) 2903–2912.
[28] A. Zunger, Phys. Rev. B 22 (1980) 5839–5872.
[29] A. Zunger, Phys. Rev. Lett. 44 (1980) 582–586.
[30] J.R. Chelikowsky, J.C. Phillips, Phys. Rev. B 17 (1978) 2453–2477.
[31] M.L. Cohen, J. Phys. Colloque (C8) (1984) 7–11.
[32] L.M. Hoistad, Inorg. Chem. 34 (1995) 2711–2717.
[33] S. Lee, Acc. Chem. Res. 24 (1991) 249–254.
[34] D.G. Pettifor, R. Podloucky, Phys. Rev. Lett. 53 (1984) 1080–1083.
[35] The moment method has been previously used in treating the AuCu$_3$ structure. See: Carlsson, A.E. Phys. Rev. B 1991, 43, 12176–12186. In the previous work, this analysis has focused on the effect of bond angles on the fourth moment. In this paper, where we consider the differences of energy of AuCu$_3$ and Cr$_3$Si structures, we find that these bond angles have a negligible effect; instead the numbers of triangles and squares of bonded atoms play a dominant role.
[36] J.K. Burdett, S. Lee, J. Amer. Chem. Soc. 107 (1985) 3050–3063.
[37] D. Pettifor, Bonding and Structure in Molecules and Solids, Oxford University Press, Oxford, 1995.
[38] E. Todorov, M. Evans, S. Lee, R. Rousseau, Chem. Eur. J. 7 (2001) 2652–2662.
[39] H.P.J. Wijn (Ed.), Landolt–Börnstein Numerical Data and Functional Relationships in Science and Technology, New Series, Group III, vol. 19, subvolume A: 3d, 4d and 5d Elements, Alloys and Compounds, Springer-Verlag, Berlin, 1986.
[40] G.A. Landrum, YAeHMOP: Yet Another extended Hückel Molecular Orbital Package, Version 2.0b.; YAeHMOP is freely available on the WWW at URL: http://sourceforge.net/projects/yaehmop/.
[41] S. Karlin, L.S. Shapley, Mem. Amer. Math. Soc. 12 (1953) 1.
[42] J.K. Burdett, S. Lee, J. Am. Chem. Soc. 107 (1985) 3063.
[43] G. Kresse, J. Hafner, Phys. Rev. B 47 (1993) 55.
[44] G. Kresse, J. Hafner, Phys. Rev. B 49 (1994) 14251.
[45] G. Kresse, J. Furthmüller, Comput. Mater. Sci. 6 (1995) 15.
[46] G. Kresse, J. Furthmüller, Phys. Rev. B 54 (1996) 11169.
[47] H.J. Monkhorst, J.F. Pack, Phys. Rev. B 13 (1976) 5188.
[48] D. Vanderbilt, Phys. Rev. B 41 (1990) 7892.
[49] U. Müller, Inorganic Structural Chemistry, Wiley, New York, 1993, pp. 140–141.
[50] W.B. Pearson, The Crystal Chemistry and Physics of Metals and Alloys, Wiley-Interscience, New York, 1972.
[51] In Fig. 11, we use the μ_n^0 set of moments (Appendix A), as we are interested in the Wolfsberg–Helmholtz approximation, an energy equation normally expressed in eV.
[52] L.M. Hoistad, S. Lee, J. Amer. Chem. Soc. 113 (1991) 8216–8220.